A. Khansili, A. Bangura, R. D. McDonald, B. J. Ramshaw, A. Rydh, and A. Shekhter<sup>3, \*</sup>

<sup>1</sup>Department of Physics, Stockholm University, SE-106 91 Stockholm, Sweden

<sup>2</sup>National High Magnetic Field Laboratory, Tallahassee FL 32310

<sup>3</sup>Los Alamos National Laboratory, Los Alamos NM 87545

<sup>4</sup>Laboratory of Atomic and Solid State Physics, Cornell University, Ithaca NY 14853 USA

(Dated: April 2, 2023)

Quasiparticle density of states in correlated and quantum-critical metals directly probes the effect of electronic correlations on the Fermi surface. Measurements of the nuclear spin-lattice relaxation rate provide one such experimental probe of quasiparticle mass through the electronic density of states. By far the most common way of accessing the spin-lattice relaxation rate is via nuclear magnetic resonance (NMR) and nuclear quadrupole resonance (NQR) experiments, which require resonant excitation of nuclear spin transitions Here we report non-resonant access to spin-lattice relaxation dynamics in AC-calorimetric measurements. The nuclear spin-lattice relaxation rate is inferred in our measurements from its effect on the frequency dispersion of the thermal response of the calorimeter-sample assembly. We use fast, lithographically-defined nanocalorimeters to access the nuclear spin-lattice relaxation times in metallic indium from 0.3 K to 7 K and in magnetic fields up to 35 T.

In nuclear magnetic resonance (NMR) and nuclear quadrupole resonance (NQR) experiments, the nuclear spin transitions are excited resonantly by radio-frequency (RF) pulses. To measure the nuclear spin-lattice relaxation rate, the first RF pulse takes nuclear spins out of their equilibrium with the electrons on the Fermi surface and lattice excitations (phonons), and the second pulse probes their relaxation toward equilibrium [1–4]. By applying the heat load on the lattice, nuclear spin transitions can be excited non-resonantly by the same spin-lattice interactions that are responsible for nuclear spin relaxation towards equilibrium. With fast calorimeters, one can resolve the dynamics of the heat flow between the lattice and the nuclear spins, as manifest in the delayed temperature response of the lattice to the heat load.

Because of the large mismatch between nuclear- and electronic energy-level splittings in a magnetic field, the nuclear spin-lattice relaxation times in elemental metals are extremely slow compared to other microscopic timescales [4], ranging from 5 ms in thallium at 1 K, 100 ms in indium and palladium, and 1 to 50 seconds for most other metals. These timescales can be accessed in small calorimeters. The slow spin-lattice relaxation dynamics determines the characteristic time delay between the temperature of the calorimeter and the heat load on the heater. Equivalently, the spin-lattice relaxation shows up as the characteristic time in the frequency dependence of the complex thermal impedance of the calorimeter-sample assembly.

The specific heat of the nuclear spins (nuclear Schottky) and the specific heat of the lattice (electrons + phonons) can be determined *independently* by such "thermal impedance spectroscopy" (TISP), because they are distinguished by their time-delayed response rather than by their magnitude. This presents a significant ad-

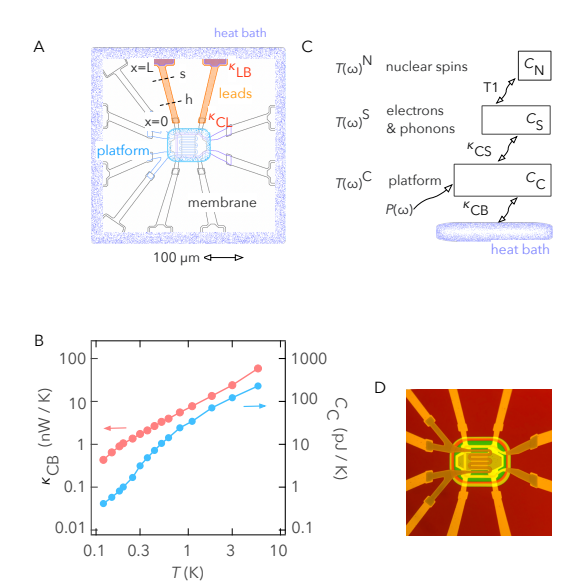


FIG. 1. Nanocalorimeter setup. A. Sketch of the components of the nanocalorimeter. B. Thermal conductance of calorimeter-heat-bath heat link  $\kappa_{\rm CB}$  and heat capacity of the calorimeter platform  $C_{\rm C}$ . The ratio of  $C_{\rm C}/\kappa_{\rm CB}$  is an indicator of the characteristic time of the calorimeter platform, ranging from 1 ms to 2 ms between 0.1 K and 1 K. C. The heat flow diagram of the calorimeter-sample assembly. The sample is thermally coupled to the calorimeter platform via a thin layer of grease with contact conductance  $\kappa_{\rm CS}$ . D. Optical image of the nanocalorimeter. The gold-capped chromium leads are 400  $\mu$ m long, 35  $\mu$ m wide, and 60 nm thick. The 1 x 1 mm<sup>2</sup> SiN membrane is 150 nm thick [5, 6].

vantage, compared to the traditional, "static" specific heat measurements, where the two are superimposed. Compared to NMR and NQR measurements, the nonresonant excitation of nuclear spins in TISP experiments puts less stringent requirements on the homogeneity of the internal and external magnetic fields. Here we report TISP measurement of the nuclear spin-lattice relaxation rate in metallic indium.

Our lithographically-defined nanocalorimeter consists of a 150 nm-thick, 1x1 mm<sup>2</sup> SiN membrane with a  $100 \times 100 \ \mu \text{m}^2$  calorimeter platform at the center [5, 6]. The platform contains a calorimeter stage, heater, and thermometer, all in fast thermal contact with each other (Figure 1A,D). The thermal link to the heat bath is provided by gold-capped chromium leads (Figure 1A,D). The strength of the link is approximately 10 nW/K at 1 K and increases approximately linearly with the temperature between 0.1 K to 10 K (Figure 1A). The heat capacity of the calorimeter platform is 10 pJ/K at 1 K and increases approximately linearly with temperatures between 1 K and 10 K (Figure 1B). The nominal characteristic time of such a calorimeter, given by the ratio of the heat capacity of the calorimeter platform and the thermal conductance of the thermal link, is 1 ms. On a millisecond time scale, the calorimeter stage, thermometer, and heater act as a monolithic calorimeter platform with uniform temperature  $T(t)^{C}$  measured by the thermometer (Figure 1A,D). A metallic indium sample of mass 1.7  $\mu$ g (15 nmol) is mounted on the calorimeter platform using a thin layer of grease.

We drive an oscillating heat load,  $P(\omega)$  (Figure 1C), and measure the complex (both in-phase and out-of-phase) temperature response of the calorimeter platform,  $T(\omega)^{\rm C}$ . This defines a complex thermal impedance [7, 8] of the calorimeter-sample assembly,  $\zeta(\omega)^{\rm C} = T(\omega)^{\rm C}/P(\omega)$ . Figure 2A shows the observed thermal impedance of the metallic indium sample in the frequency range of 10 mHz to 1 kHz plotted in the complex plane of  $\zeta^{\rm C}$ . Figure 1C shows the different components that make up the thermal response of the calorimeter. The thermal impedance corresponding to the heat flow diagram in Figure 1C is given by

$$\frac{1}{\zeta(\omega)^{C}} = \kappa_{CB} - i\omega C_{C} + \frac{-i\omega \left(C_{S} + \frac{C_{N}}{-i\omega T l + 1}\right) \kappa_{SC}}{-i\omega \left(C_{S} + \frac{C_{N}}{-i\omega T l + 1}\right) + \kappa_{SC}},$$
(1)

where  $\kappa_{\rm SC}$  is the thermal conductance of the contact between the calorimeter platform and the sample,  $\kappa_{\rm CB}$  is the thermal conductance from the calorimeter platform to the heat bath, T1 is the nuclear spin-lattice relaxation time, and  $C_{\rm C,S,N}$  are heat capacities of the calorimeter platform, and electron+phonon and nuclear spin subsystems in the sample, respectively. Eq. (1) faithfully describes the heat circuit in Figure 1C below 3 kHz, set by the thermal diffusion time across the leads, 50  $\mu$ s at 1 K. At higher frequencies, the frequency dispersion of the thermal link  $\kappa_{\rm CB}(\omega)$  needs to be accounted for (Meth-

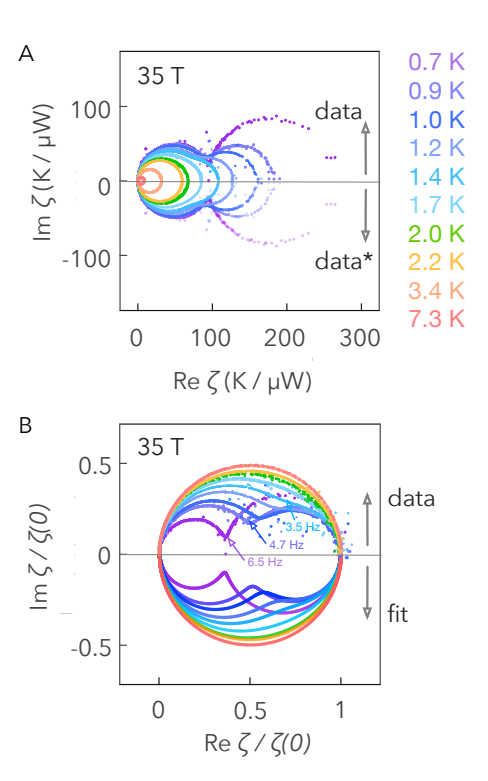


FIG. 2. The thermal impedance of the calorimeter-sample assembly in the complex plane of  $\zeta$ . A. Measured thermal impedance  $\zeta(\omega)$  at 35 T at temperatures in the range 0.7 K to 8 K. The upper half  $\mathrm{Im}\zeta>0$ , shows the observed thermal impedance. The lower half,  $\mathrm{Im}\zeta<0$ , is added as a guide for the eye to represent the thermal impedance at negative frequencies,  $\zeta(-\omega)=\zeta^*(\omega)$ . B. The normalized thermal impedance  $\zeta(\omega)/\zeta(\omega=0)$  where  $\zeta(\omega=0)=1/\kappa_{\mathrm{CB}}$ . The upper half of the plot shows the observed normalized thermal impedance. The lower half shows the fit to Eq. (1) with fitting parameters discussed in Figure 3A.

ods).

The thermal impedance in Eq. (1) is a superposition of three complex Lorentzians,  $\zeta(\omega) = \sum_{i=1,2,3} A_i/[-i\omega+1/m_i]$ , all centered at zero frequency. The amplitudes  $A_{1,2,3}$  are real and characteristic times, denoted  $m_{1,2,3}$ , are all positive, by causality. The temperature dependencies of  $m_{1,2,3}$  obtained from the data in Figure 2 are shown as gray lines in Figure 3A. The two longer characteristic times,  $m_1$  and  $m_2$ , span the interval from 1 sec to 1 ms in the temperature interval from 0.2 K to 7 K. The measurement frequency range encompasses the two longer characteristic times  $m_1$  and  $m_2$  in this temperature interval.

We can define three timescales using parameters in Eq. (1),  $\tau_{\rm S} = C_{\rm S}/\kappa_{\rm CB}$ ,  $\tau_{\rm C} = C_{\rm C}/\kappa_{\rm CB}$ , and  $\tau_{\rm N} = C_{\rm N}/\kappa_{\rm CB}$ . Figure 3A shows the temperature dependence of  $\tau_{\rm S}, \tau_{\rm C}, \tau_{\rm N}$  determined by the fit of the observed frequency dependence to Eq. (1) at each temperature and

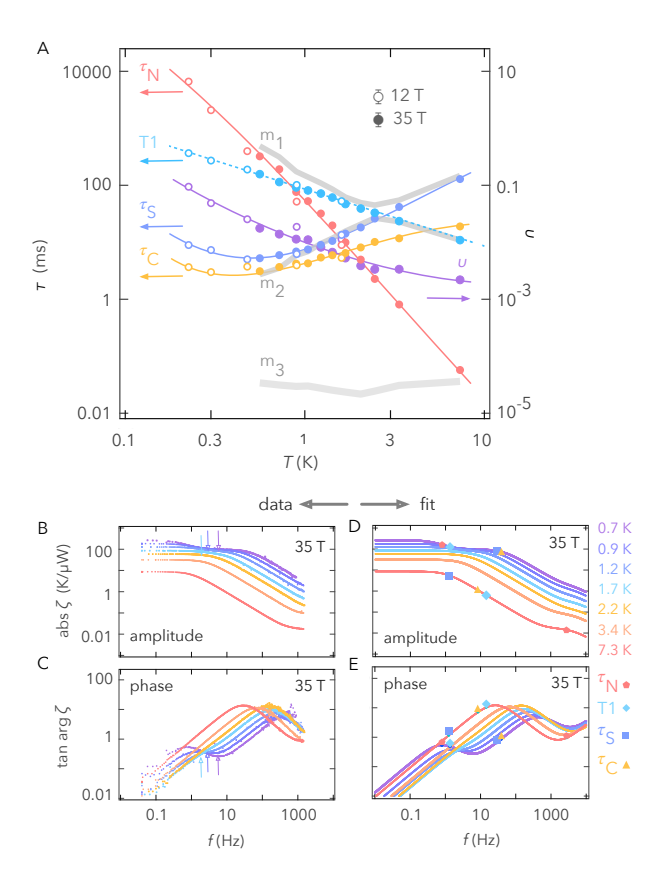


FIG. 3. Fitting the thermal impedance of the calorimetersample assembly. A. The temperature dependence of the fitting parameters  $\tau_{\rm S} = C_{\rm S}/\kappa_{\rm CB}$ ,  $\tau_{\rm C} = C_{\rm C}/\kappa_{\rm CB}$ ,  $\tau_{\rm N} = C_{\rm N}/\kappa_{\rm CB}$ , the nuclear spin-lattice time, T1, and a dimensionless ratio  $v = \kappa_{\rm CB}/\kappa_{\rm SC}$ , determined by the fit to Eq. (1). The filled circles represent measurements in the resistive magnet at 35 T on a 15 nmol-size sample. The open circles represent measurements in the superconducting magnet at 12 T on 7.8 nmol sample. The nuclear Schottky for the 12 T measurements is scaled by a factor  $(35/12)^2$ . Thick gray lines represent the characteristic times  $m_1$ ,  $m_2$ , and  $m_3$  of the calorimeter-sample assembly determined by the observed thermal impedance via  $\zeta(\omega) = \sum_{i=1,2,3} A_i/[-i\omega + 1/m_i]$ . The dashed cyan line indicates the nuclear spin-lattice time T1 measured in NQR experiments [9, 10]. Solid lines tracing  $\tau_{S,N,C}$  and v are guide for the eye. B,C. Frequency dependence of the polar components (amplitude and phase) of the observed thermal impedance in the frequency range of 10mHz to 1 kHz. D,E. Frequency dependence of polar components of  $\zeta(\omega)$  in Eq. (1) with the best-fit parameters from A. The values of parameters  $\tau_{\rm C,S,N}$ and T1 are indicated by markers at  $f = 1/(2\pi\tau_{C,S,N})$  on top of 7.3 K and at 0.7 K frequency scans.

magnetic field (Methods).

At higher temperatures, the sample and the calorimeter platform are in thermal equilibrium. In this low-frequency regime, the thermal impedance in Eq. (1) reduces to a single-characteristic-time form used in AC-calorimetric measurements [5, 6, 11–13],  $\zeta(\omega)^{\rm C}=$ 

 $1/[\kappa_{\rm CB} - i\omega(C_{\rm C} + C_{\rm S} + C_{\rm N})]$ . At 7 K, this low-frequency regime extends up to about 20 Hz, which is the inverse of the second-largest characteristic time at that temperature (Figure 3A). The plateauing of the amplitude at 7 K below about 1 Hz (red curve in Figure 3B) corresponds to the longest characteristic time  $m_1$  at 7 K (Figure 3A). This low-frequency regime corresponds to a large circle in the complex plane of  $\zeta^{\rm C}$ , defined by the Lorentzian  $A_1/[-i\omega+1/m_1]$  with the longest characteristic time  $m_1$  shown in Figure 2B where we plot the normalized value of the thermal impedance  $\zeta(\omega)^{\rm C}/\zeta(\omega=0)^{\rm C}$ .

As we lower the temperature, internal thermal equilibrium between the calorimeter platform and the sample, and between the electron-phonon and nuclear-spin subsystems of the sample, breaks down. The multirelaxation-time character of the frequency dependence of the thermal impedance in this regime is evident in the "multi-circle" geometry of the frequency traces of  $\zeta(\omega)$ in the complex plane (Figures 2A,B). At 0.7 K the two resonances in  $\zeta(\omega)^{C}$  are clearly visible in the amplitude plot (Figure 3B). The plateau below 30 Hz corresponds to a broad resonance with a characteristic time of 5 ms, the intermediate characteristic time  $m_2$  in Figure 3A at 0.7 K, which is close to  $\tau_{\rm C}$  and  $\tau_{\rm S}$  at that temperature. The plateau in the amplitude below 0.3 Hz (purple curve in Figure 3B) corresponds to the longest characteristic time of 0.5 sec in Figure 3A at 0.7K.

Figure 4A shows the specific heat of the nuclear spin (in red) and lattice (electrons + phonons, in blue) subsystems, as extracted from the data shown in Figure 2 using the model given by Eq. (1). The specific heat of metallic indium, measured in Ref. 14, is shown as a dashed blue line in Figure 4A. Naturally-occurring indium has two isotopes:  $^{115}\text{In}$  (95.7%) and  $^{113}\text{In}$  (4.3%). Both isotopes have nuclear spin J=9/2 and g-factors differing by 0.2%,  $^{115}g_{\rm N}=+1.231$  and  $^{113}g_{\rm N}=+1.229$  [15]. At low magnetic fields,  $\mu_{\rm N}B\ll k_{\rm B}T$ , the nuclear Schottky per mol is  $c_{\rm N}=(1/3)\,J(J+1)N_{\rm A}k_{\rm B}\,(g_{\rm N}\mu_{\rm N}B/k_{\rm B}T)^2$  where  $\mu_{\rm N}=32.5$  neV/T is the nuclear magneton. For elemental indium, this is shown as a dashed red line in Figure 4A.

The nuclear spin-lattice interactions in metallic indium have been studied previously in the NQR [9, 10, 16, 17] and NMR [18, 19] experiments. Figure 4B shows the nuclear spin-lattice relaxation rate 1/T1T determined by the fits of Eq. (1) to the data in Figure 2. The dashed line shows the value of T1T = 0.086 s K from NQR experiments [9, 10].

We now briefly discuss the thermodynamic description of nuclear spins, as it relates to TISP experiments. In a metal, the spin temperature is established by spin-spin interactions on the timescale of spin-spin relaxation time, T2 of the order of 1 - 100  $\mu$ s [4, 20, 21], faster than T1 in a typical metal. In indium metal, T2 = 100  $\mu$ s [10].

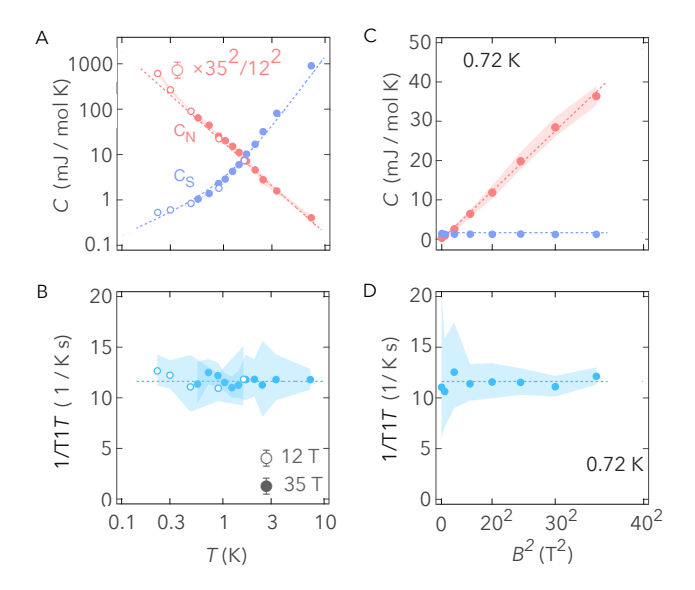


FIG. 4. Temperature and magnetic field dependence of the spin-lattice relaxation rate and nuclear- and lattice heat capacity. A. Magnetic field dependence of the nuclear Schottky  $C_{\rm N}$  (in red) and electronic specific heat  $C_{\rm S}$  (in purple) at 0.7 K. Magnetic field axis scales as field-squared. The shaded region around the line represents the error bars (Methods). B. The nuclear spin-lattice relaxation rate 1/T1T vs field. C. Temperature dependence of the nuclear Schottky  $C_N$  (per mol) and the electronic (+ phonon) specific heat  $C_{\rm S}$  (per mol) at 35 T (filled circle markers) and 12 T (open circles). For the sake of comparison, the nuclear Schottky at 12 T is scaled up by a factor  $(35/12)^2$ . The dashed blue line indicates heat capacity measured in Ref. 14,  $c_S = (1.69 \text{ mJ} / \text{mol K}^2) T +$  $(1.43 \text{ mJ} / \text{mol K}^4) T^3$ . The dashed red line indicates the expected magnitude of the nuclear Schottky in indium metal,  $c_N = (0.015 \text{ mJ K} / \text{mol T}^2) B^2/T^2$ . D. Temperature dependence of the nuclear spin-lattice relaxation rate 1/T1T at 35 T (filled circle markers) and 12 T (open circles).

Thus, the nuclear spin temperature is well-defined on the timescale of 1 ms. The non-uniform spatial dependence of the nuclear spin- and lattice temperatures need not be similar to each other, despite the fact that the spin-lattice interaction is local. This is because the heat can flow "laterally" between the nuclear spins mediated by spin-spin interaction and across the lattice, mediated by heat diffusion. The (lattice) heat diffusion time across the cuboid-shape sample of mass 1.7  $\mu$ g is short, about 10 ns (Methods). Therefore, in our measurement, both the lattice  $T_{\rm S}$  and the spin  $T_{\rm N}$  temperatures are uniform across the sample in our measurements, as assumed in Eq. (1).

Different isotopes of the same nucleus will be out of equilibrium with each other when an oscillating heat load is applied to the lattice because spin-spin relaxation is ineffective in establishing the common temperature for isotope species when energy-matching conditions between them are broken. Indium, however, is peculiar in this respect: the g-factors of its two naturally occurring isotopes,  $^{113}\mathrm{In}$  and  $^{115}\mathrm{In}$ , differ by only 0.2%. At low magnetic fields, the nuclear-spin energy levels of the two isotopes effectively overlap due to finite width effects. The nuclear-spin energy states are broadened by inelastic energy exchange mediated by either the spin-spin or the spin-lattice interactions. In metals, the energy transfer mediated by the spin-spin interactions, dominates these effects[4, 21, 22]. In metallic indium, the width of the nuclear energy states,  $\sim \hbar/T2$ , is comparable with the energy mismatch of its two isotopes in applied magnetic fields of 10 T or smaller.

Regardless, the detection of partial thermal equilibrium between indium isotopes in metallic indium requires a sub-percent-level of determination of T1, beyond our current sensitivity (Figure 4B). The partial equilibrium between different isotopes (or different lattice sites with different Knight shifts) might be an important consideration in other systems (Methods).

Finally, the spin-lattice time T1 is defined in Eq. (1) via effective "contact" thermal conductance between nuclear-spin and the lattice,  $\kappa_{\rm SN}^{\rm eff} = C_{\rm N}/T1$ . To establish a connection between the TISP measurements and the NMR and NQR experiments [4, 21, 22], we consider the energy exchange between the nuclear spins and the lattice. Approach to thermal equilibrium is governed by the relaxation dynamics of the entropy  $[23, 24], d(S_N + S_S)/dt = q^{N+S} (1/T_N - 1/T_S), \text{ where}$ heat flux from the electron-phonon subsystem to the nuclear spins,  $q^{N \leftarrow S} = T_N (dS_N/dt) = -T_S (dS_S/dt)$ , is equal to the rate of change of energy of nuclear-spin subsystem,  $q^{N+S} = dQ_N/dt$ . Following Refs. (23 and 24), we chose  $x = dQ_N = C_N dT_N$  as a measure of the deviation from complete equilibrium and  $X = 1/T_{\rm N} - 1/T_{\rm S}$ as the corresponding thermodynamic force. Then the rate of change of x is proportional to the thermodynamic force,  $dx/dt = \Gamma X$ . Rewriting  $dx/dt = C_N dT_N/dt$  as  $-T_{\rm N}^2 C_{\rm N} \times d(1/T_{\rm N})/dt$  we obtain the rate equation for the nuclear temperature

$$\frac{d(1/T_{\rm N})}{dt} = -\frac{1}{T_{\rm I}} \left( \frac{1}{T_{\rm N}} - \frac{1}{T_{\rm S}} \right) \,, \tag{2}$$

where  $1/T1 = \Gamma/(T_{\rm N}^2 C_{\rm N})$  is the nuclear temperature relaxation rate. When temperature oscillations are weak,  $\delta T \ll T$ , this equation sets the effective contact thermal conductance between the nuclear spins and the lattice to  $C_N/T1$ . This establishes the equivalence of our definition of T1 in Eq. (1) and that in magnetic resonance experiments [4, 21].

The nuclear spin-lattice relaxation indicates the spinflip dynamics of electrons in the host material [1–3]. In conventional metals and in liquid  $^3$ He below 1 K [25], all spin flips occur on the Fermi surface [4, 20, 26] and the nuclear spin-lattice relaxation rate indicates the quasiparticle density of states [26] as well as the static Fermi liquid renormalization factors [25, 27–30]. Beyond conventional metals, nuclear spin-lattice relaxation probes correlation dynamics and its impact on the Fermi surface, as well as Fermi liquid renormalization factors not included in mass renormalization. One advantage of TISP measurements in this broader scientific context is that the nuclear spin-lattice relaxation rates can be measured simultaneously with electronic specific heat, thus providing two independent and complementary ways to access the quasiparticle mass or the density of states on the Fermi surface in the same measurement.

Acknowledgments. Resistive 35 T magnet measurements were performed at the National High Magnetic Field Laboratory, which is supported by the National Science Foundation Cooperative Agreement No. DMR-1644779 and the State of Florida. Work at Los Alamos National Laboratory is supported by the NSF through DMR-1644779 and the U.S. Department of Energy. A.S. acknowledges support from the DOE/BES "Science of 100 T" grant. A.S. acknowledges the hospitality of the Aspen Center for Physics, where a portion of this work was performed. Aspen Center for Physics is supported by National Science Foundation grant No. PHY-1607611. B.J.R. acknowledges funding from the National Science Foundation under grant no. DMR-1752784. A.K. and A.R. acknowledge support by the Swedish Research Foundation, D. Nr. 2021-04360.

- \* email: arkady.shekhter@gmail.com
- E. M. Purcell, H. C. Torrey, and R. V. Pound, Phys. Rev. 69, 37 (1945).
- [2] E. M. Purcell, Physica 17, 282 (1951).
- [3] N. Bloembergen, E. M. Purcell, and R. V. Pound, Physical Review 73, 679 (1948).
- [4] A. Abragam, The principles of nuclear magnetism (Oxford university press, 1961).
- [5] S. Tagliati, V. M. Krasnov, and A. Rydh, Review of

- Scientific Instruments 83, 055107 (2012).
- [6] K. Willa, Z. Diao, D. Campanini, U. Welp, R. Divan, M. Hudl, Z. Islam, W.-K. Kwok, and A. Rydh, Review of Scientific Instruments 88, 125108 (2017).
- [7] R. C. Richardson and E. N. Smith, Experimental techniques in condensed matter physics at low temperatures (CRC Press, 2018).
- [8] F. Pobell, Matter and methods at low temperatures (Springer Berlin, Heidelberg, 2007).
- [9] D. E. MacLaughlin and J. Butterworth, Physics Letters 23, 291 (1966).
- [10] D. E. MacLaughlin, J. D. Williamson, and J. Butterworth, Physical Review B 4, 60 (1971).
- [11] P. F. Sullivan and G. Seidel, Physical Review 173, 679 (1968).
- [12] J. K. Wang, J. H. Campbell, D. C. Tsui, and A. Y. Cho, Physical Review B 38, 6174 (1988).
- [13] J. K. Wang, D. C. Tsui, M. Santos, and M. Shayegan, Physical Review B 45, 4384 (1992).
- [14] H. R. ONeal and N. E. Phillips, Physical Review A 137, 748 (1965).
- [15] N. J. Stone, "table of nuclear magnetic dipole and electric quadrupole moments," (2014), Atomic Data and Nuclear Data Tables:INDC(NDS)-0658.
- [16] J. Butterworth and D. E. MacLaughlin, Physical Review Letters 20, 265 (1968).
- [17] J. D. Williamson and D. E. MacLaughlin, Physical Review B 8, 125 (1973).
- [18] J. E. Adams, L. Berry, and R. R. Hewitt, Physical Review 143, 164 (1966).
- [19] R. H. Hammond, E. G. Wikner, and G. M. Kelly, Physical Review 143, 275 (1966).
- [20] N. Bloembergen and T. J. Rowland, Acta metallurgica 1, 731 (1953).
- [21] L. C. Hebel, Solid State Physics 15, 409 (1963).
- [22] N. Bloembergen, S. Shapiro, P. S. Pershan, and J. O. Artman, Physical Review 114, 445 (1959).
- [23] L. Onsager, Physical Review 37, 405 (1931).
- [24] L. Onsager, Physical Review 38, 2265 (1931).
- [25] A. J. Leggett, Reviews of Modern Physics 47, 331 (1975).
- [26] J. Korringa, Physica 16, 601 (1950).
- [27] L. D. Landau, Sov. Phys. JETP 3, 920 (1957).
- [28] A. J. Leggett, Annals of Physics 46, 76 (1968).
- [29] A. G. Anderson and A. G. Redfield, Physical Review 116, 583 (1959).
- [30] T. Moriya, Journal of the Physical Society of Japan 18, 516 (1963).